

# Experimental Investigation of a Hydrofoil Designed via Hydrostructural Optimization

Nitin Garg<sup>a</sup>, Bryce W. Pearce<sup>b</sup>, Paul A. Brandner<sup>b</sup>, Andrew W. Phillips<sup>c</sup>, Joaquim R. R. A. Martins<sup>d</sup>, Yin L. Young<sup>a,1</sup>

<sup>a</sup>*Department of Naval Architecture and Marine Engineering, University of Michigan, MI, USA*

<sup>b</sup>*Australian Maritime College, University of Tasmania, Launceston, TAS, Australia*

<sup>c</sup>*Maritime Division, Defence Science and Technology Group, Fishermans Bend, VIC, Australia*

<sup>d</sup>*Department of Aerospace Engineering, University of Michigan, MI, USA*

---

## Abstract

In the last decade, there has been an increased interest in the use of multidisciplinary optimization techniques for the design of aerospace, maritime, and wind engineering systems. However, validation of numerically optimized results using experimental measurements has been scarce. In this paper, numerical predictions are compared with experimental measurements of the hydrodynamic forces, deformations, and cavitation performance for a baseline NACA 0009 hydrofoil and an optimized hydrofoil. Both hydrofoils are made of solid aluminum, and are cantilevered at the root. One of the hydrofoils is optimized using a high-fidelity hydrostructural solver combined with a gradient-based optimizer, as detailed by Garg et al. [1]. The numerical predictions agree well with experimental measurements for both the baseline NACA 0009 and the optimized hydrofoils. For the optimized hydrofoil, the mean differences between the predicted and measured values for mean lift, drag coefficient, and moment coefficients, are 2.9%, 5.1%, and 3.0%, respectively. For the non-dimensional tip bending deflection, the mean difference is 3.4%. Although the optimized hydrofoil is significantly thicker to withstand higher loads than the baseline, it yields an overall measured increase in the lift-to-drag ratio of 29% for lift coefficients ranging from  $-0.15$  to  $0.75$  and exhibits significantly delayed cavitation inception compared to the baseline. The improvement in hydroelastic and cavitation performance is attributed to the changes in the distribution of camber, twist, thickness, and the leading edge radius of the optimized hydrofoil. The results validate the analysis and optimization of the high-fidelity hydrostructural design optimization approach, and opens up new possibilities for the design of high-performance hydrofoils, marine propellers, and turbines.

**Keywords:** Experimental, Numerical, High-fidelity Hydrostructural, Multidisciplinary design optimization, Fluid-structure interaction, Cavitation

---

## Nomenclature

$\alpha$  Geometric angle of attack [deg]

---

<sup>1</sup>Corresponding author, email address for correspondence: [ylyoung@umich.edu](mailto:ylyoung@umich.edu)

$\nu_s$	Solid Poisson's ratio
$\rho_s$	Solid density [ $\text{kg}/\text{m}^3$ ]
$\sigma$	Cavitation number, $\sigma = \frac{P_{\text{ref}} - P_{\text{vap}}}{0.5\rho_f U^2}$
$\sigma_v$	Maximum von Mises stress [MPa]
$\sigma_{s,f}$	Fatigue strength [MPa]
$\sigma_y$	Yield strength [MPa]
$a$	Speed of sound in the fluid [m/s]
$c$	Hydrofoil mean chord [m]
$C_D$	Drag coefficient, $C_D = \frac{D}{0.5\rho_f U^2 sc}$
$C_L$	Lift coefficient, $C_L = \frac{L}{0.5\rho_f U^2 sc}$
$C_L/C_D$	Lift-to-drag ratio or hydrodynamic efficiency
$C_M$	Pitching moment coefficient, $C_M = \frac{M}{0.5\rho_f U^2 sc^2}$
$C_p$	Pressure coefficient, $C_p = \frac{P_{\text{local}} - P_{\text{ref}}}{0.5\rho_f U^2}$
$KS_{\sigma_v}$	Non-dimensional aggregated stress constraint
$P_{\text{local}}$	Local fluid pressure [Pa]
$P_{\text{ref}}$	Reference upstream hydrostatic pressure [Pa]
$P_{\text{vap}}$	Saturated vapor pressure of the fluid [Pa]
$Re$	Reynolds number, $Re = Uc/\nu_f$
$s$	Hydrofoil span [m]
$t_{\max}$	Local maximum hydrofoil thickness [m]
$t_{\max}/c$	Maximum thickness-to-chord ratio
$U$	Inflow velocity [m/s]
$U_{\text{cav}}$	Cavitation inception speed, $U_{\text{cav}} = \sqrt{\frac{P_{\text{ref}} - P_{\text{vap}}}{0.5\rho_f C_{p_{\min}}}} \text{ [m/s]}$
$A_{\text{cav}}$	Non-dimensional aggregated cavitation constraint
$A_{\text{ref}}$	Reference hydrofoil area [ $\text{m}^2$ ]

## 1. Introduction

Recently, there has been an increased interest in the use of multidisciplinary optimization (MDO) techniques [2] for maritime applications, including the design of advanced material hulls [3, 4, 5, 6], and marine propulsors [7, 8, 9, 10]. However, experimental validation of optimized designs has been limited. When using MDO, it is well known that numerical optimization will exploit any weakness in the numerical model, the optimization problem formulation, or both. Therefore, to obtain practical engineering designs, it is necessary to validate numerical predictions with experimental measurements [11]. Moreover, it is also important to understand the design changes that lead to the performance improvement to facilitate future designs.

Garg et al. [1] performed the first high-fidelity hydrostructural design optimization with respect to large numbers of shape variables. The hydrostructural solver coupled a Reynolds-averaged Navier–Stokes (RANS)-based solver with a finite element analysis (FEA) solid solver to account for the interdependent fluid-structure interaction response. The solver was combined with a gradient-based optimization algorithm, and they used a coupled-adjoint approach [12, 13] to compute the required gradients efficiently. The combination of numerical techniques enabled efficient hydrostructural shape optimization with respect to over 200 shape design variables while enforcing cavitation constraints, structural failure constraints, and manufacturing tolerances to achieve a practical engineering design. The optimization is for a canonical hydrofoil or a rudder that is expected to operate over a wide range of loading conditions. For practical applications, the objective function and design constraints vary depending on the specific application. Since this is an academic study with no specific target application vessel, the objective function we applied in the multipoint optimization is based on the typical desire to minimize drag, avoid cavitation, and ensure structural integrity. The assumed range of operating conditions is very broad, with lift coefficients ranging from -0.15 to 0.75, and the most frequent operating condition corresponds to a lift coefficient of 0.65. Garg et al. [1] found that the hydrostructural optimization lead to completely different optimized geometry than the hydrodynamic-only optimized design, and that only the hydrostructural optimized design satisfied the structural stress constraints at high loading conditions. However, they validated the hydrostructural solver against the experimental measurements for the baseline aluminum NACA 0009 hydrofoil only, and not for the optimized hydrofoil.

Various experimental studies of non-optimized (canonical or baseline) flexible hydrofoils and propellers in cavitating and sub-cavitating flows can be found in the literature [14, 15, 16, 17, 18, 19, 20]. However, experimental validation studies of numerically optimized marine lifting bodies has been very limited. Lin et al. [7] carried out one of the first published experimental studies of optimized composite propellers. They performed experimental studies in a cavitation tunnel for three composite DTNSRDC 4498 propellers with different stacking sequence of fiber reinforced plastic (FRP) layers: 1) the original propeller geometry with quasi-isotropic stacking sequence, 2) the original propeller geometry with the optimized stacking sequence, obtained using genetic algorithm [21, 22], and 3) a pre-deformed propeller geometry with the optimized stacking sequence. The optimized propeller was designed to have a torque coefficient equal to that of the original propeller geometry at a design advance coefficient of  $J = 0.889$ . However, the experimental data showed that the design torque was not met at this advance coefficient for the original propeller geometry with the optimized stacking sequence. Results also showed poor agreement between the experimental measurements and numerical predictions using a steady-state boundary element method solver coupled with the commercial finite element solver ABAQUS for all the three pro-

80 pellers. They also did not consider structural integrity or cavitation in the optimization study, and structural performance was not reported in the experimental study. Recently, Herath et al. [23, 24] used a genetic algorithm to optimize a composite hydrofoil for the layup sequence. The objective function was to achieve the ideal required change in twist under the difference in pressure caused by the change in angle of attack and the choice of the material layup sequence. The experimental results showed that the optimized hydrofoil maintained a higher lift-to-drag ratio around its operating point compared to the baseline hydrofoil. However, Herath et al. [23, 24] did not optimize the geometric shape of the hydrofoil and also did not consider cavitation performance nor the maximum stress constraints.

In the current paper, we address the need for more experimental verification of coupled hydrostructural design optimization results by presenting the first experimental study of the hydroelastic and cavitation performance for both the baseline NACA 0009 hydrofoil and the multipoint hydrostructural optimized hydrofoil across a wide range of lift conditions. The goals of this work are to: 1) validate the high-fidelity multipoint hydrostructural design optimization with experimental measurements; and 2) highlight the reason for significant improvement in performance by the optimized hydrofoil.

90 The remainder of this paper is organized as follows. We start by briefly summarizing the numerical methodology and optimization problem formulation used to obtain the coupled hydrostructural optimized hydrofoil in Sections 2 and 3. In Section 4, we describe the experimental setup and techniques, including the hydrofoil geometry. Section 5 compares the modal shapes and frequencies of the baseline and the optimized hydrofoil. Section 6.1 focuses on the numerical results from the multipoint hydrostructural optimization, while Section 6.2 compares the predicted and measured hydroelastic and cavitation performance of the baseline and the optimized hydrofoils. Finally, our findings are summarized in Section 7.

100 It should be noted that while the baseline and optimized hydrofoil geometries are the same as shown in Garg et al. [1], the numerical results shown in this work are generated using a much finer fluid and structural mesh than those used in [1]. The finer mesh are found to be necessary for accurate comparison with experimental measurements, particularly in the drag predictions. Hence, we present the predicted results with the finer mesh along with the experimental measurements for the baseline and the optimized hydrofoil.

## 2. Numerical Methodology

The hydrostructural optimization framework used in this work is extended from previously developed framework, MACH (MDO of Aircraft Configurations with High-fidelity) [13, 25, 26]. The details of the hydrostructural framework are described previously by Garg et al. [1], but they are summarized here for completeness.

### 2.1. CFD Solver

110 The CFD solver used is ADflow, which is a 3-D finite-volume, cell-centered multi-block solver for the compressible flow equations [27]; and can compute the gradients using an adjoint method. The RANS equations with the Spalart–Allmaras (SA) [28] turbulence model are used for the work herein. A low-speed preconditioner was previously implemented in ADflow to solve hydrodynamic problems involving nearly incompressible flows for Mach numbers as low as 0.01 [29, 30]. An aggregated non-dimensional cavitation constraint was implemented previously [1]. We only

placed a constraint in the optimization to avoid cavitation by ensuring that the predicted total absolute pressure is greater than the saturated vapor pressure, but there is no cavitation model to simulate the evolution of cavitation. The Jameson–Schmidt–Turkel [31] scheme augmented with artificial dissipation is used for spatial discretization. An explicit multi-stage Runge–Kutta method is used for the temporal discretization.

## 2.2. Structural Solver

120 The structural solver used in the MACH framework is the Toolkit for the Analysis of Composite Structures (TACS) [32]. TACS is a parallel, general 3-D FEA solver for structural analysis that can also compute gradients using an adjoint method, making the cost of the gradient calculation nearly independent of the number of structural design variables. The stress constraint is computed using the Kreisselmeier–Steinhauser (KS) constraint aggregation technique [33, 34], which provides a conservative estimate of the maximum stress in a smooth and differentiable manner.

## 2.3. Fluid-Structure Coupling Algorithm

The CFD and the structural solvers described above are coupled to predict the hydrodynamic loads, solid stresses, and deformations for a given flow condition. The hydrodynamic loads (pressure and shear stresses) computed by ADflow are transferred to the structural solver, and the displacements from the structural solver, in turn, dictate the CFD mesh movement. Rigid links are used to extrapolate the displacements from the structural surface to the CFD surface. The integration of the forces is performed on the CFD mesh, and the forces are then transferred to the structure through the rigid links. The details of the load and displacement transfer scheme used in the hydrostructural optimization can be found in Brown [35] and Kenway et al. [13].

130 To solve the coupled hydrostructural equations, the hydrodynamic analysis is first partially converged, and the forces are evaluated. These forces are then transferred to the structural analysis, and the corresponding displacements are computed. Thereafter, the displacements are transferred back to the hydrodynamic analysis, the geometry and the corresponding mesh is deformed, and a new CFD solution is found. This iterative loop continues until the coupled convergence criterion is satisfied (when the relative decrease in both the aerodynamic and structural residuals compared to the free-stream values is less than  $10^{-5}$ ).

## 2.4. Geometry Perturbation Algorithm

The free-form deformation (FFD) volume approach was used to parameterize the geometry [13]. To obtain a more efficient and compact set of geometric design variables, the FFD volume approach parameterizes the geometric changes rather than the geometry itself. All the geometric changes are performed on the outer boundary of the FFD volume. Changes to this outer boundary modify the objects embedded in the volume, including the hydrofoil and the structural mesh, and hence will affect the structural performance in addition to the hydrodynamic performance.

## 2.5. Optimization Algorithm and Adjoint Gradient Computation

150 As explained previously [1], we used the gradient-based optimization algorithm SNOPT (sparse nonlinear optimizer) [36] to increase the computational efficiency by minimizing the number of function evaluations (i.e., the high-fidelity hydrostructural solutions) for cases with a large number of design variables. SNOPT utilizes a sequential quadratic programming algorithm, and is capable

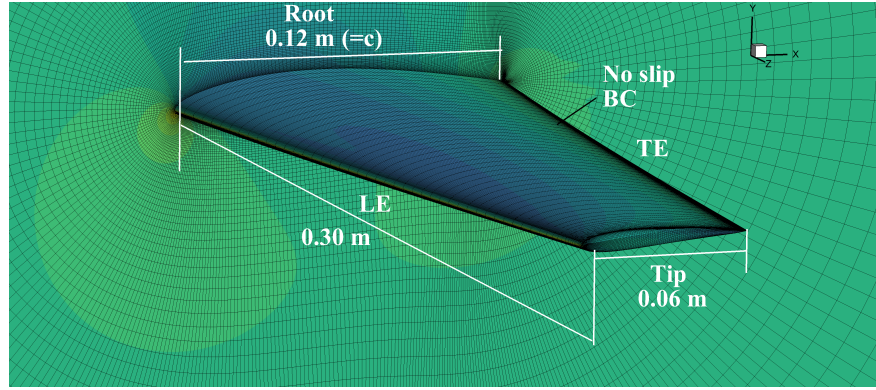
of solving large-scale nonlinear optimization problems with thousands of constraints and design variables.

An aggregation approach is required to reduce the dimensionality of the stress and cavitation constraints so that the adjoint method is advantageous, as explained in previous work [34, 1].

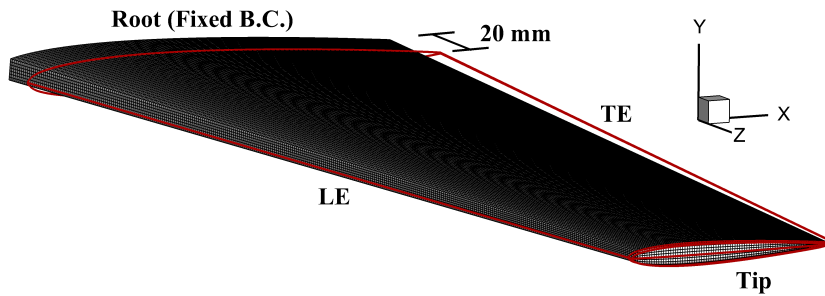
### 3. Optimization Problem Formulation

The numerical model presented in this work is similar to the one presented earlier by Garg et al. [1], except that much finer CFD and FEM meshes are used in this paper. The fluid and structural grid convergence study for the case is already presented earlier in Garg et al. [1]. The geometry is a cantilevered NACA 0009 hydrofoil made of solid aluminum. Figure 1(a) represent the CFD mesh used in this paper. The CFD mesh is a structured O-grid with 4,124,160 cells and  $y^+ = 0.9$ . The domain size is 30 chord lengths in all directions.

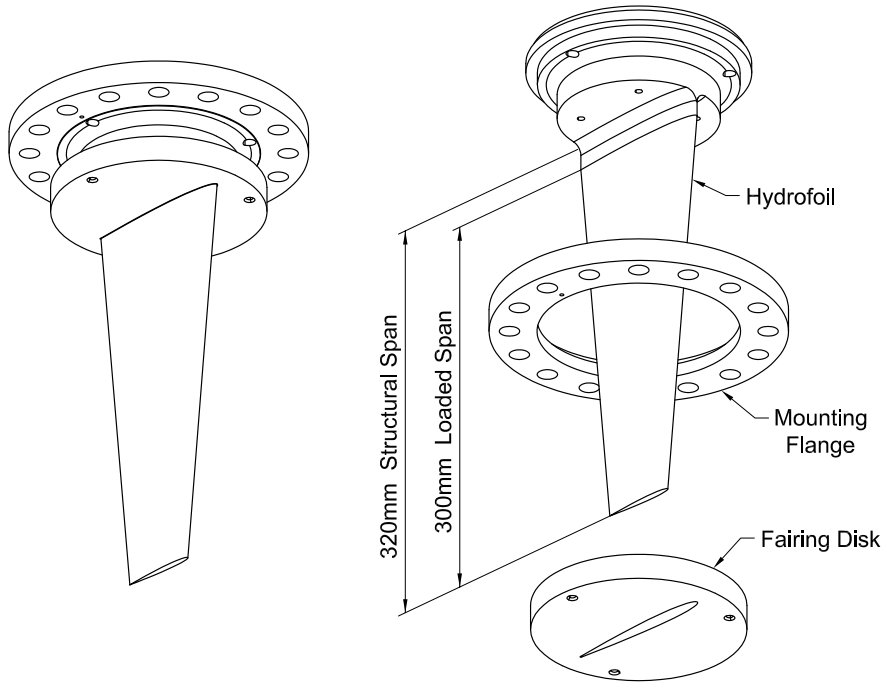
Figure 1(b) shows the structural mesh used for the optimization and the validation results. The structural mesh has 179,200 linear 8-node brick elements, with 9 elements along the thickness direction, 80 elements in the chordwise direction, and 240 elements in the spanwise direction.



(a) CFD mesh and geometry



(b) Structural mesh



(c) Hydrofoil mounting arrangement for the baseline and the optimized hydrofoils.

Figure 1: Baseline cantilevered NACA 0009 hydrofoil and the hydrofoil mounting arrangement. Figures (a) and (b) illustrate the CFD and FEA mesh, respectively, used in the predictions shown in this work. Figure (c) illustrates the hydrofoil mounting set up, and the difference between the loaded span length (300 mm) and the structural span length (320 mm).

Table 1: Hydrofoil design optimization problem.

	Function/ variables	Description	Quantity
minimize	$\bar{C}_D$	Weight-averaged drag coefficient	1
with respect to	$x$	FFD control points Twist design variables	200 10
subject to	$C_L^*$ $A_{\text{cav}} \leq 5 \times 10^{-4}$ $KS_{\sigma_v} \leq 1$ $t_{TE_i} \geq 1.1t_{TE_{\text{base}}}$	Target lift coefficient constraints Fixed leading edge constraint Non-dimensional aggregated cavitation constraint Stress constraint Trailing edge thickness constraint	5 10 5 5 20

The optimization problem formulation is the same as defined by Garg et al. [1] and is summarized in Table 1 and briefly described here for completeness. The assumed weights at the five  
 170 lift conditions are 0.10, 0.15, 0.25, 0.45, and 0.05 at  $C_L = -0.15, 0.30, 0.50, 0.65$ , and 0.75, respectively.

The objective of the numerical optimization is to minimize the weighted average of the drag coefficient over a range of lift conditions.

$$\bar{C}_D = \sum_{k=1}^m w_k C_{D_k} \quad (1)$$

where the weights  $w_k$  are computed based on the probability of operation at a given  $C_L$ ,  $p(C_{L_k})$ , i.e.,  $w_k = p(C_{L_k}) \Delta C_L$ .

The overall hydrodynamic efficiency is defined as

$$\bar{\eta} = \sum_{k=1}^m w_k \frac{C_{L_k}}{C_{D_k}}. \quad (2)$$

Constraints are imposed on the lift coefficients, minimum pressure coefficient (cavitation), and maximum von Mises stress on the five operating conditions defined in Garg et al. [1]. The  
 180 cavitation constraint is required to be satisfied over all the CFD cells representing the hydrofoil surface, and the maximum stress constraint is required to be satisfied over all the FEM elements representing the hydrofoil volume. Additional constraints were imposed on minimum thicknesses at the hydrofoil trailing edge for manufacturability and ease of handling. The trailing edge thickness is constrained to be at least 10% higher than the baseline NACA 0009 hydrofoil thickness at 20 points distributed spanwise along the trailing edge. The leading edge position and chord length are fixed to the baseline NACA 0009 hydrofoil values.

Figure 2 shows the 200 FFD control points used for optimization. The total number of design variables is 210, which includes 200 FFD control points (10 spanwise  $\times$  10 chordwise  $\times$  2 thickness), and 10 spanwise twist design variables—as shown in Figure 2.

The twist design variables are defined as the angle of a given section relative to the root section,

190 and the angle of attack is the angle of the root cross section relative to the free stream. To ensure a consistent definition of the angle of attack when comparing the performance of the baseline and the optimized hydrofoils at a given lift, we subtract the twist at the root from all the outboard sections. Hence, all the geometric angles of attack and twist angles shown in Section 6 are defined relative to the root section, and the twist at the root section is zero.

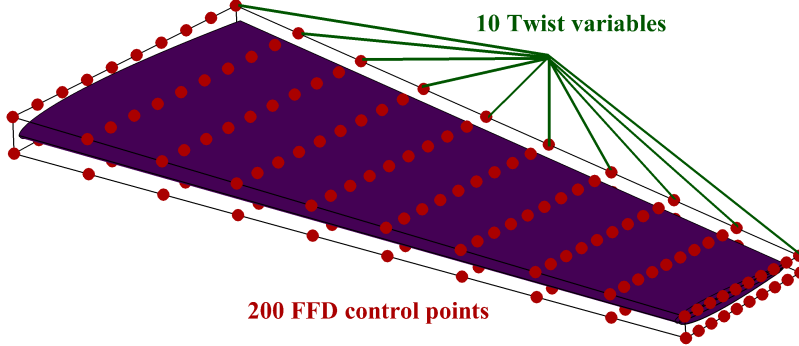


Figure 2: The hydrostructural optimization design variables consist of 200 FFD control points (red spheres) and 10 section twist variables [1].

#### 4. Experimental Setup and Techniques

In this section, we describe the experimental facility, hydrofoil setup, and the experimental techniques. Both the baseline hydrofoil, and the optimized hydrofoil are manufactured by the Defence Science and Technology Group (DST), Australia, and are tested in the Cavitation Research Laboratory (CRL) variable pressure tunnel at the Australian Maritime College (AMC), Tasmania.

##### 200 4.1. Experimental Facility

The detailed explanation of the experimental facility can be found in previous work [37, 38, 15] and is only described briefly here. The tunnel test section is 0.6 m square by 2.6 m long. The operating velocity range is 2–12 m/s, and the pressure range is 4–400 kPa of absolute pressure. The test section velocity is spatially uniform to within 0.5%, has temporal variations of less than 0.2%, and the freestream turbulence intensity at the inlet of the test section is about 0.5%. The measurements uncertainties of the various parameters are listed in Table 2. The force and velocity measurements are used to compute the various hydrodynamic coefficients, such as, lift coefficient, drag coefficient, and moment coefficient. The highest estimated uncertainty of the tip deflection are at the lowest angle of attack because of the low deformations and the measurement uncertainty of 0.648 mm in the tip deflection.

##### 210 4.2. Baseline Hydrofoil

As explained by Zarruk et al. [15], the baseline hydrofoil geometry has an unswept trapezoidal planform with a loaded span of 300 mm, a base chord of 120 mm, and a tip chord of 60 mm. The hydrofoil is rigidly mounted from the ceiling of the test section via a six-component force balance (described in Section 4.4). The effective aspect ratio of the hydrofoil, considering the double body effect created by the cantilevered condition at the root, is 6.67, and the mean chord is 90 mm.

Table 2: Experimental measurement uncertainties for critical model parameters.

Parameter	Uncertainty
Velocity	0.007 m/s (low-range) and 0.018 m/s (high-range)
Force (load cell)	0.5%
$C_L$ , $C_D$ , and $C_M$	0.95% (low-speed) – 1.2% (high-speed)
Angle of attack	0.1°
Tip deflection ( $\delta_{tip}$ )	14.53% ( $\alpha = 2^\circ$ ) – 3.33% ( $\alpha = 10^\circ$ ) for $Re = 1 \times 10^6$

The baseline hydrofoil is made up of standard symmetric NACA 0009 section profiles. The experimental hydrodynamic characteristics of the NACA 0009 profiles are extensively described in the literature [39, 40]. Two geometrically identical metal baseline NACA 0009 hydrofoils were manufactured and tested: one made of solid stainless steel or steel (316L alloy) and the other made of solid aluminum (6061-T6 alloy). The steel baseline hydrofoil served as the rigid baseline, as it undergoes negligible deformation. Since the aluminum hydrofoil is more flexible and undergoes measurable tip bending deflection, we use it as the baseline for the hydrostructural optimization. Based on the construction and attachment assembly of the hydrofoil shown in Figure 1(c), the structural span is 320 mm (as opposed to the 300 mm loaded span) for both the baseline and optimized hydrofoils. The steel and aluminum hydrofoils were manufactured to a  $\pm 0.1$  mm surface tolerance and a  $0.8 \mu\text{m}$  surface finish. No roughness was added to induce turbulent flow, as the laminar flow region should be limited for the NACA 0009 section [41].

#### 4.3. Optimized Hydrofoil

The optimized hydrofoil is manufactured from solid aluminum alloy (6061-T6), which was the same as the aluminum baseline hydrofoil. The alloy properties are listed in Table 3. Pictures of the steel baseline and the multipoint hydrostructural optimized aluminum hydrofoil models are shown in Figure 3. Figure 4 compares the sectional geometry of the baseline and the optimized hydrofoils at ten sections along the span. The results show an increased thickness in the optimized hydrofoil, particularly near the root, to meet the stress constraint. The optimized hydrofoil also has higher camber, a different twist distribution, and rounder leading edge radius compared to the baseline to improve the hydrodynamic performance and to delay cavitation inception. Although it is not visible, the trailing edge thickness of the optimized hydrofoil is also larger than the baseline. However, minimum trailing edge thickness constraint was not sufficient to prevent the optimized hydrofoil from suffering two small chips on the trailing edge due to the challenges with manufacturing and handling a highly cambered hydrofoil with a still relatively thin trailing edge. These discrepancies emphasize the importance of including manufacturing and handling tolerances, as well as uncertainty due to manufacturing in the optimization problem formulation. Nevertheless, since the two small chips are localized and did not affect the twist and camber distribution, they had negligible impact on the hydroelastic performance of the hydrofoil, as will be shown later in the Section 6.

#### 4.4. Experimental Techniques

The hydrofoils were mounted via a six-component force balance through a 0.16 m diameter penetration on the tunnel test section ceiling 0.7 m downstream of the test section entrance. The

Table 3: 6061-T6 aluminum alloy material properties.

Symbol	Description	Value	Units
$\rho_s$	Solid density	2700	kg/m <sup>3</sup>
$E_s$	Elastic modulus	69	GPa
$\nu_s$	Poisson's ratio	0.33	–
$\sigma_y$	Yield strength	276	MPa
$\sigma_{s,f}$	Fatigue strength	97	MPa



Figure 3: Photographs of the baseline steel and optimized aluminum hydrofoils used in experiments, along with the mounting arrangement.

250 details for the mounting arrangement are already presented in [15, 42]. Data were sampled at 1 kHz for 30 s for all the Re values. The estimated precision of all 6 force balance components has an uncertainty of less than 0.5%. The uncertainty in the absolute position of the indexing system is

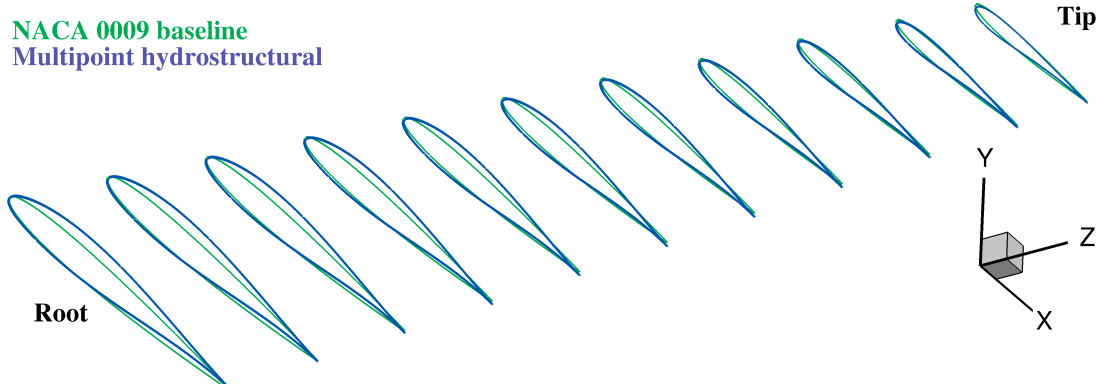


Figure 4: Comparison of sectional geometries for the NACA 0009 baseline, and the multipoint optimized design at ten sections along the span. The optimization increases the thickness (particularly near the root) to meet the stress constraint, it increases the leading edge radius to delay cavitation inception, and it adds camber and twist to improve hydrodynamic performance across the wide range of lift conditions, with lift coefficients ranging from -0.15 to 0.75.

less than  $0.1^\circ$ . The experimental tip bending deflection presented in this paper involves processing the images of the hydrofoil tip section in unloaded and loaded conditions using the Matlab [43] ‘imfindcircles’ algorithm. The known hydrofoil tip chord was used to calibrate the images and the worst case uncertainty was found to be 0.65 mm, based on the diameter of the contrasting targets. The details of the procedure are already presented in [42].

## 5. Modal Analysis

We study the effective stiffness of the baseline and the optimized hydrofoils by comparing the natural frequencies of the two hydrofoils. The natural frequencies also help to understand the vibration characteristics of the hydrofoil, which is needed to avoid unwanted vibration, noise, hydroelastic instability, and accelerated fatigue [11].

Figure 5 shows the first four in-air modes and their corresponding frequencies for the baseline aluminum and the multipoint optimized aluminum hydrofoil, predicted using the in-house structural solver, TACS. The results show that the frequencies for the optimized hydrofoil are significantly higher than the baseline. The higher frequencies are expected since the optimized hydrofoil has thicker cross-sections (as shown in Figure 4). The first three in-air mode shapes of the baseline and optimized hydrofoil are similar, however, the fourth mode shape differs significantly. While the fourth mode of the baseline aluminum hydrofoil is the lead-lag mode, the fourth mode of the optimized aluminum hydrofoil is the second twisting mode, as a result of the thicker cross-sections.

## 6. Results

In this section, we first present the numerical results obtained using the fine CFD and FEA meshes shown in Figure 1, followed by comparison of the numerical predictions with experimental measurements for the hydrodynamic performance, deformation response, and cavitation performance for both the baseline aluminum NACA 0009 hydrofoil and the multipoint hydrostructural optimized aluminum hydrofoil.

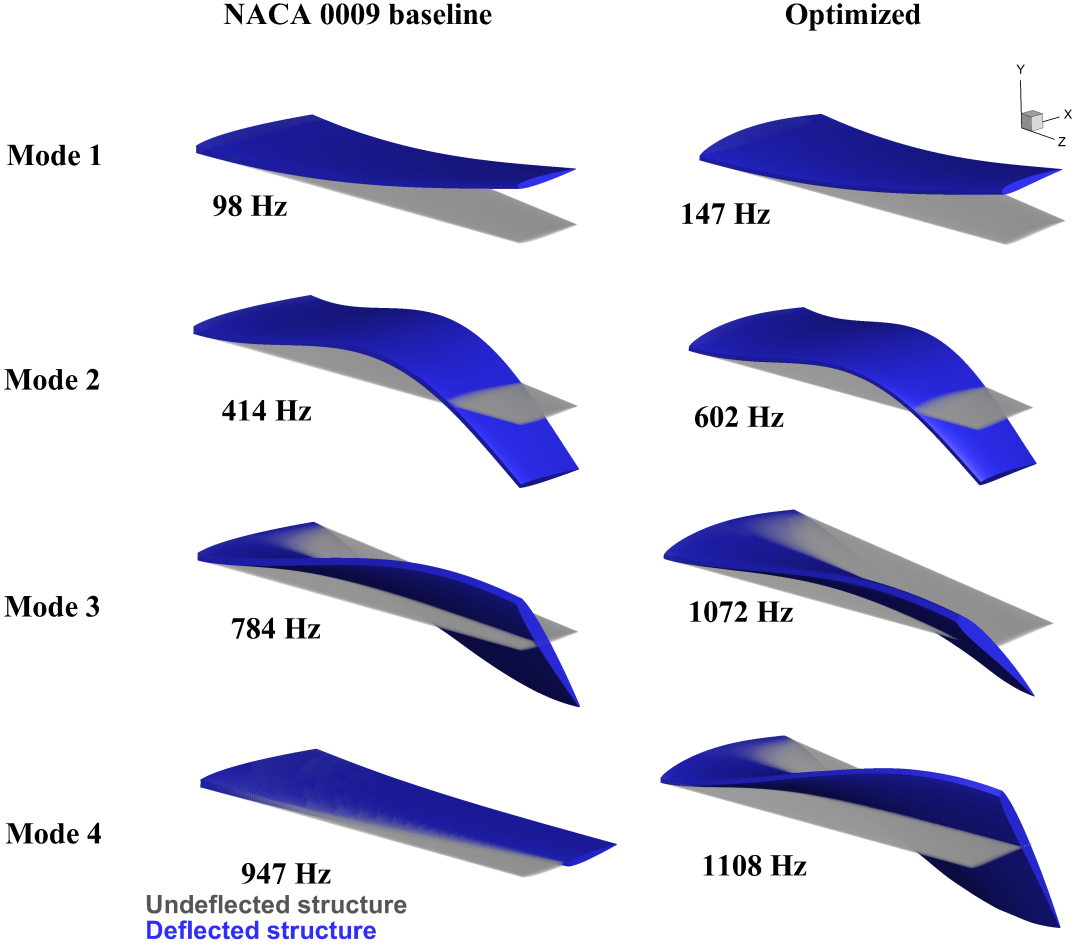


Figure 5: First four in-air natural vibration modes and frequencies for the baseline aluminum and the multipoint optimized aluminum hydrofoil. The undeformed geometry is shown using the light gray mesh, while the deformed mode shapes are shown in the solid blue mesh. The thicker cross-sections resulted in significantly higher frequencies of the optimized hydrofoil compared to the baseline hydrofoil.

### 6.1. Numerical Results for Multipoint Hydrostructural Optimization

Although the multipoint hydrostructural optimization geometry is the same as presented by Garg et al. [1], the numerical results presented here are obtained with finer CFD and FEA meshes of 4,124,600 cells and 179,200 elements, respectively. In [1], coarser CFD and FEA meshes with 515,200 cells and 44,800 elements, respectively, were used in the optimization study.

The drag convergence study presented previously [1] for the NACA 0009 baseline showed that a CFD mesh of 4,124,160 cells and a structural mesh of 179,200 are necessary to achieve the drag convergence, which yielded a mean difference between predictions and measurements for lift force and moment coefficient prediction to be 3.5%, and the mean difference in the drag coefficient to be 5.4%. Garg et al. [1] also compare  $C_L$ ,  $C_M$ ,  $C_D$ , and  $\delta_{tip}/s$  from a coarser CFD mesh (515,520 cells) and a coarser structural mesh (44,800 elements). The results show that while the  $C_D$  is over-predicted by 45.6% (mean) compared to the fine mesh predictions, the mean difference in  $C_L$  and  $C_M$  is 4.4%. Additionally, the  $C_D$  predicted using the coarser mesh (515,520 cells) follow the same trend as the finer mesh (4,124,160 cells) and the experimental measurements. The

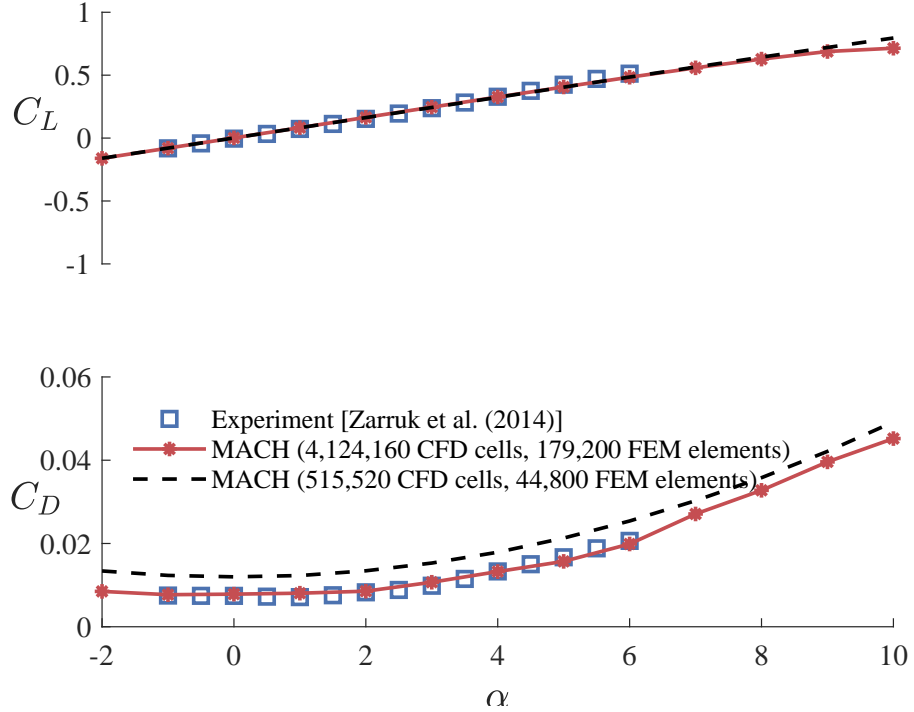


Figure 6: Comparison between lift coefficient and drag coefficient from two different sets of meshes, and experimental results of the baseline aluminum NACA 0009 hydrofoil at  $Re = 10^6$  [15]. Red solid line represents results from finer CFD and FEA meshes (used for all the results presented in this paper) and black dashed line represents results from coarser CFD and FEA meshes (used for the optimization studies presented in [1]).

results are illustrated in Figure 6, which compares  $C_L$  and  $C_D$  for the finer CFD and FEA meshes, coarser CFD and FEA meshes, and the experimental results from Zarruk et al. [15] for the baseline NACA 0009 hydrofoil. Since the adjoint-based hydrostructural shape optimization is concerned with the trend of the drag coefficient with changes in geometry, the actual grid converged value is not as important. Hence, for the sake of computational efficiency, the coarser CFD mesh with 515,520 cells and a structural mesh with 44,800 elements was used for the coupled multipoint optimization studies presented by Garg et al. [1]. In the present work, since absolute values are critical for accurate validations with experimental measurements, we used the finer CFD mesh of 4,124,160 cells and structural mesh of 179,200 elements for all the numerical results. Additionally, as shown in Garg et al. [1], the difference between the efficiency at  $C_L = 0.48$  obtained using the current mesh with 4,124,160 CFD cells and 179,200 FEM elements and the next finer mesh with 10,158,720 CFD cells and 179,200 FEM elements is only 0.2%, which is negligible compared to the predicted 25% efficiency improvement for the optimized hydrofoil compared to the baseline at  $C_L = 0.5$ . For comparison, the measured efficiency improvement is 31% at  $C_L = 0.5$ .

Figure 7 compares the multipoint hydrostructural optimized hydrofoil to the baseline NACA 0009 hydrofoil at two extreme operating conditions, i.e.,  $C_L = -0.15$  and  $C_L = 0.75$ , and the most frequent operating point,  $C_L = 0.65$ . The baseline aluminum hydrofoil is shown on the left and the optimized aluminum hydrofoil is shown on the right of each subplot. As presented in [1], the optimized design is driven by efficiency, stress at the highest loading condition, i.e.,  $C_L = 0.75$ , and the cavitation constraint at the negative  $C_L$  condition, i.e.,  $C_L = -0.15$ . The mass of the baseline aluminum hydrofoil is 0.41 kg and the mass of the optimized aluminum hydrofoil is 0.58 kg. Even

with the higher mass caused by the thicker cross-sections, the multipoint optimized hydrofoil lead to a predicted increase in the overall efficiency (Eq. (2)) of 31.3% for operation across  $C_L$  ranging from  $-0.15$  to  $0.75$ , and a maximum increase in efficiency of 43.7% at  $C_L = 0.75$ , compared to the NACA 0009 baseline. Figure 7 shows the  $C_p$  contours on the pressure side for  $C_L = -0.15$  (the pressure-side cavitation-critical condition), the  $C_p$  distribution on the suction side for  $C_L = 0.65$  (the efficiency-critical condition) and  $C_L = 0.75$  (the strength and suction-side cavitation-critical condition). Additionally, the figure shows the stress constraint value, i.e.,  $1.1\sigma_v \leq \sigma_{s,f}$ , on the suction side for the highest loading condition, i.e.,  $C_L = 0.75$ .  $\sigma_v$  is the maximum von Mises stress and  $\sigma_{s,f}$  is the fatigue strength of aluminum.

The  $C_L = 0.65$  and  $C_L = 0.75$  pressure contours show that partial leading-edge cavitation is present in the baseline design, while the optimized design does not exhibit any cavitation, both at  $\sigma = 1.6$ . The results show an increase in cavitation inception speed by 38% at  $C_L = 0.65$  for an assumed submerged depth of 1 m over the NACA 0009 baseline. The cavitation inception speed,  $U_{\text{cav}}$ , is defined as,

$$U_{\text{cav}} = \sqrt{\frac{P_{\text{ref}} - P_{\text{vap}}}{0.5\rho_f C_{p_{\min}}}} \quad (3)$$

where  $P_{\text{ref}} = P_{\text{atm}} + \rho_f gh$  is the reference pressure,  $P_{\text{atm}}$  is the atmospheric pressure,  $\rho_f$  is the fluid density,  $g$  is the gravitational acceleration,  $h$  is the submerged depth, and  $P_{\text{vap}}$  is the vapor pressure of water at 15°C (1706 Pa). The optimizer avoids cavitation in the process of reducing the drag by increasing the leading edge radius while adding camber and twist, as shown in Figure 4.

The contour of the von Mises stress,  $\sigma_v$ , normalized by the fatigue strength, as well as the initial (unloaded) and deformed geometry, for both hydrofoils at  $C_L = 0.75$  are shown at the bottom of Figure 7. The baseline hydrofoil violates the stress constraint for  $C_L \geq 0.35$  (see Figure 11), and undergoes much more significant deformation due to the reduced stiffness as a result of the lower cross-sectional thickness.

The multipoint optimization has to satisfy the stress and cavitation constraint at two extreme design conditions ( $C_L = 0.75$  and  $C_L = -0.15$ ), which requires thickening both the inboard and outboard portions of the hydrofoil, leading to a 41% mass increase over the NACA 0009 baseline (as shown in Figure 4).

Figure 8 plots the sectional pressure profile for the baseline hydrofoil and the optimized hydrofoil at three sections along the span. Figure 8 shows that at the  $C_L = -0.15$  condition, the suction peak of the optimized hydrofoil is just under the  $\sigma = 1.6$  cavitation constraint line for the outer profiles ( $z/s = 0.6, 0.8$ ), indicating that the cavitation constraint at this condition is active and has a direct effect on the design. The results also show that the baseline hydrofoil violates the cavitation constraint at higher  $C_L$  values of 0.65 and 0.75, while the optimized hydrofoil satisfies the cavitation constraint ( $-C_{p_{\min}} < (\sigma = 1.6)$ ) at both the positive and the negative lift conditions.

Figure 9 compares the ideal elliptical lift distribution with the lift distribution for the baseline and the optimized hydrofoils for two extreme operating conditions, i.e.,  $C_L = -0.15$  and  $C_L = 0.75$ , and the most frequent operating point, i.e.,  $C_L = 0.65$ . The lift distribution for the symmetrical NACA 0009 baseline hydrofoil remains nearly identical for both positive and negative lift coefficients, and all deviate from the ideal elliptical distribution with the maximum efficiency based on potential flow assumptions. On the other hand, the lift distribution for the cambered optimized hydrofoil at  $C_L = 0.65$  and  $C_L = 0.75$  are very closely to the elliptical loading distribution. The lift distribution of the optimized hydrofoil deviates from the elliptical distribution only at the

low probability operation point of  $C_L = -0.15$ .

Figure 10 compares the drag distribution for the baseline and the optimized hydrofoil for two extreme operating conditions, i.e.,  $C_L = -0.15$  and  $C_L = 0.75$ , and the most frequent operating point, i.e.,  $C_L = 0.65$ . Note the higher drag for the baseline hydrofoil, especially at the root and tip, for the efficiency-critical operating point, i.e.,  $C_L = 0.65$ . The higher total drag for the baseline hydrofoil is also indicated in the Table 4.

360 Figure 11 compares the maximum stress constraint values over the hydrofoil, i.e.,  $1.1\sigma_v \leq \sigma_{s,f}$ , for the NACA 0009 baseline and the optimized hydrofoil. While the baseline NACA 0009 hydrofoil violates the stress constraint for  $C_L \geq 0.35$ , the optimized hydrofoil satisfies the stress constraint up to the highest loading condition ( $C_L = 0.75$ ) because of the thicker cross-sections, particularly near the root where the stresses are the highest.

In summary, the numerical results show that the multipoint optimized hydrofoil was found to perform significantly better than the baseline NACA 0009 hydrofoil in terms of the lift-to-drag ratio, while meeting cavitation, stress, and manufacturing constraints [1]. In the next subsections, we validate these performance improvements against experimental measurements.

Table 4: Comparison of the predicted drag coefficient values for the baseline and the optimized hydrofoil at the three different lift conditions.

Operating point ( $C_L$ )	Baseline ( $C_D$ )	Optimized ( $C_D$ )
-0.15	0.008	0.007
0.65	0.035	0.025
0.75	0.046	0.032

## 6.2. Experimental Validation

370 In this section, we compare the numerical predictions against the experimental measurements for lift, drag, and moment coefficients, tip deflections, as well as cavitation performance.

### 6.2.1. Hydroelastic Performance

Figure 12 compares the numerical predictions and the experimental measurements for  $C_L$ ,  $C_D$ , and  $C_M$  at various angles of attack. The open square symbols and circle symbols represent the experimental measurements, while the lines represent the numerical predictions. The blue square symbols and blue solid lines represent the optimized hydrofoil, the green circle symbols and green dashed lines represent the baseline hydrofoil. As explained earlier, since the absolute values of  $C_L$  and  $C_D$  are critical for the validation studies, the numerical predictions shown in this paper are carried out with the finer CFD and FEA meshes with 4,124,600 cells and 179,200 elements, respectively, for both the baseline and the optimized hydrofoils. As shown in Figure 12 and Table 5, good agreement between the numerical predictions and the experimental measurements are observed.

The predicted and measured tip bending deflection ( $\delta_{tip}$ ) for both the baseline and the optimized hydrofoils are shown in Figure 13. The bending deflection is non-dimensionalized by the mean semi chord ( $\delta_{tip}/b$ ), where  $b = 45$  mm. The mean difference in the tip deflections is 3.45%. The tip twists are not compared, since the twist for the aluminum hydrofoil is too small to measure.

Figure 14 compares the drag polar for the baseline NACA 0009 hydrofoil and the optimized hydrofoil. The results show that for a given  $C_L$ , the optimized hydrofoil has a lower  $C_D$  than

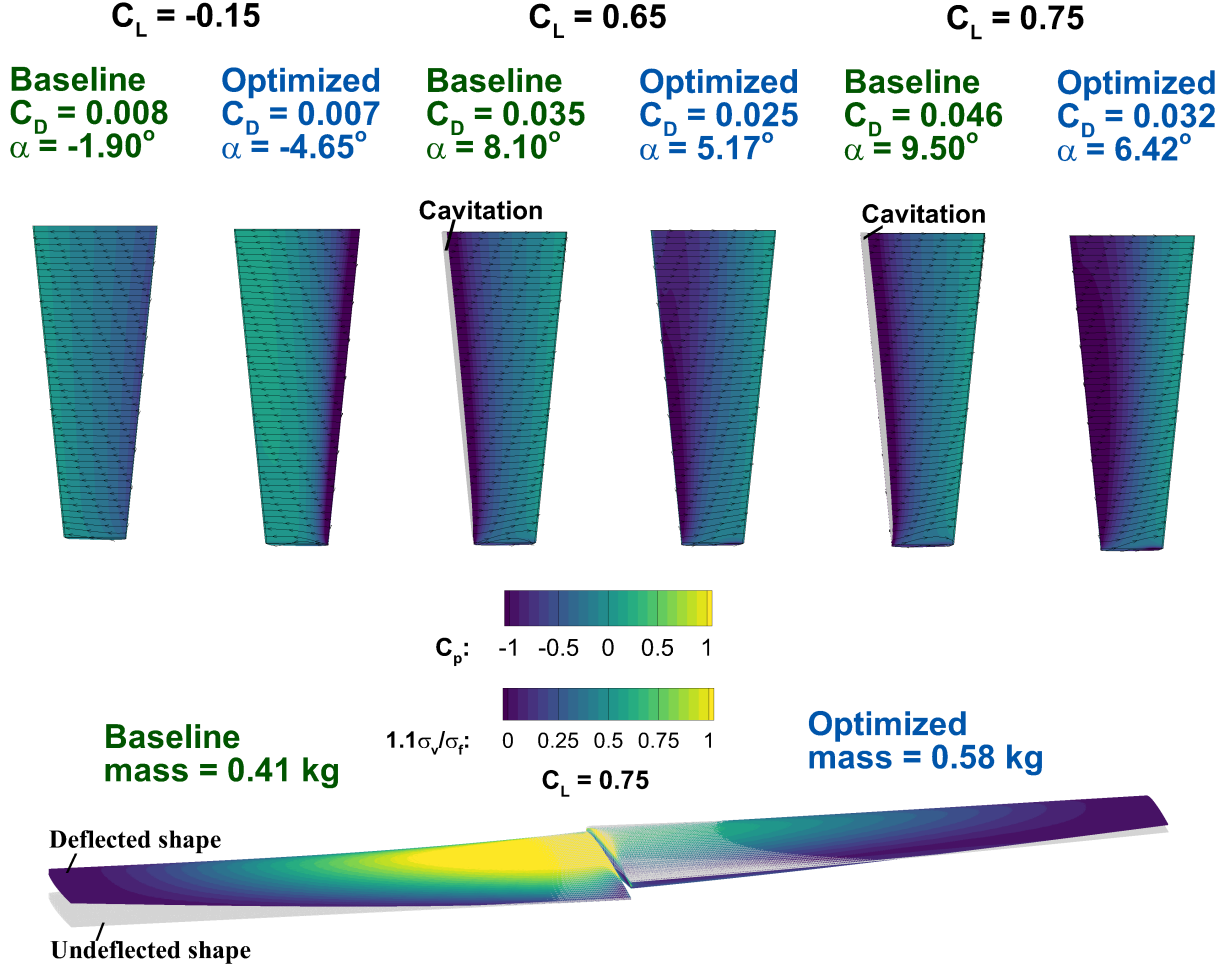


Figure 7: Comparison between the multipoint hydrostructural optimized hydrofoil (blue or dark) and the aluminum NACA 0009 baseline hydrofoil (green or light). The predicted overall lift-to-drag ratio increased by 31.3% and the maximum increase on efficiency is 43.7% at  $C_L = 0.75$ . It is impressive that the optimized hydrofoil lead to such significant increase in efficiency even with a mass increase by 41% (due to the thicker cross-sections) compared to the NACA 0009 baseline. The baseline hydrofoil violates the stress constraint for  $C_L \geq 0.35$  (see Figure 11), and undergo much more significant deformation due to a lower cross-sectional thickness (see Figure 4).

the NACA 0009 baseline hydrofoil over the entire range of operating condition. In other words,  
 390 both numerical predictions and experimental measurements show that the optimized hydrofoil performed significantly better than the baseline hydrofoil over the entire range of operating conditions. The increase in the experimental overall lift-to-drag ratio (as defined by Eq. (2)) is 29% compared to 31.3% increase in the lift-to-drag ratio from the numerical predictions. Note that the numerically predicted increase in the lift-to-drag ratio is higher than the one presented by Garg et al. [1]. This increase is due to the difference in the predicted  $C_D$  values with the coarse CFD mesh used for the optimization shown in [1] compared to the fine CFD mesh used for the analysis shown here. Figure 14 shows good agreement between the numerical predictions and experimental measurements for both the baseline and the optimized hydrofoils. The maximum, mean, and minimum differences between numerical predictions (using the 4,124,600 cell CFD mesh and the 179,200 element FEA mesh) and experimental measurements for the hydrodynamic coefficients ( $C_L$ ,  $C_D$ ,  
 400

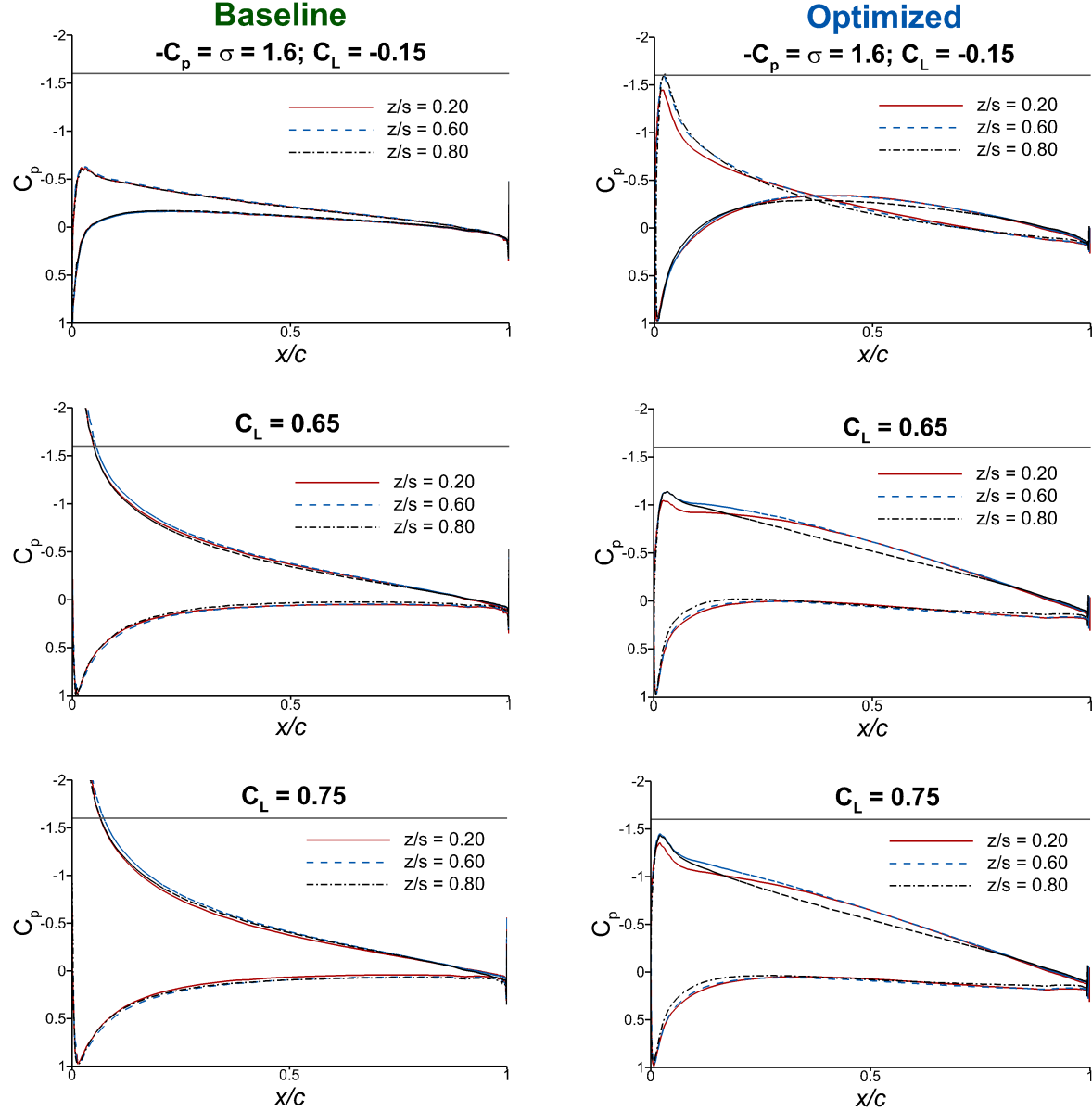


Figure 8: Comparison of the predicted sectional pressure profile for the baseline and the multipoint optimized design for three different sections along the span at  $C_L = -0.15, 0.65$ , and  $0.75$ . The gray horizontal line represents the cavitation constraint of  $\sigma = 1.6$ . The results show that while the baseline hydrofoil violates the cavitation constraint at  $C_L = 0.65$  and  $0.75$ , the optimized hydrofoil satisfies the constraint. Note that the cavitation constraint is active for  $C_L = -0.15$ .

and  $C_M$ ) and tip bending deformation ( $\delta_{\text{tip}}$ ) of the optimized hydrofoil are summarized in Table 5. Comparison of Table 2 and Table 5 shows that the mean error in the hydrodynamic coefficients is higher than the uncertainty in the measurement. However, as shown in Figures 12, 13, and 14, the predictions follow the same trend as the measurements. The adjoint-based shape optimization is more concerned with capturing the trend of the drag coefficient with changes in geometry, rather than the actual grid converged value. Thus, we concluded that the high-fidelity hydrostructural optimization tool is good enough for the purpose of the optimization, and the results are confirmed

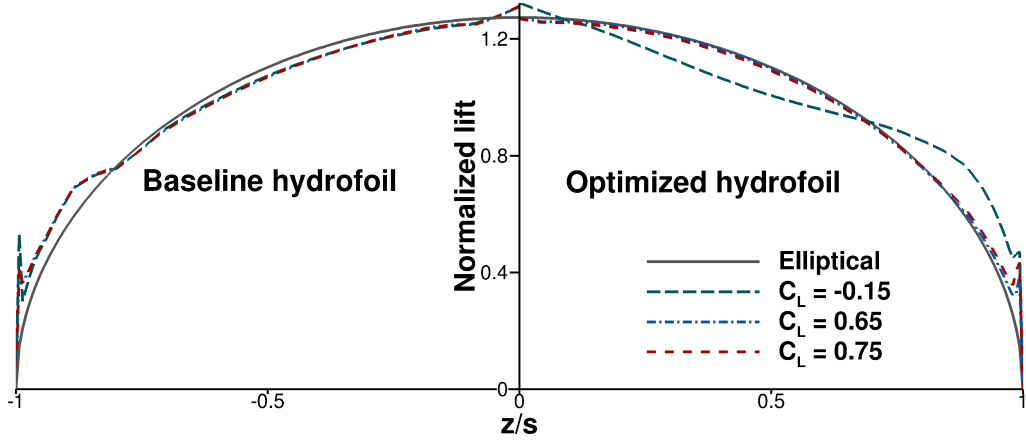


Figure 9: Comparison of the predicted spanwise normalized lift distribution for the NACA 0009 baseline, and the multipoint optimized design at  $C_L = -0.15$ ,  $C_L = 0.65$ , and  $C_L = 0.75$ . While the lift distribution for the symmetrical NACA 0009 baseline hydrofoil deviated from the ideal elliptical distribution, the lift distribution for the cambered optimized hydrofoil at  $C_L = 0.65$  and  $C_L = 0.75$  very closely followed the elliptical loading distribution.

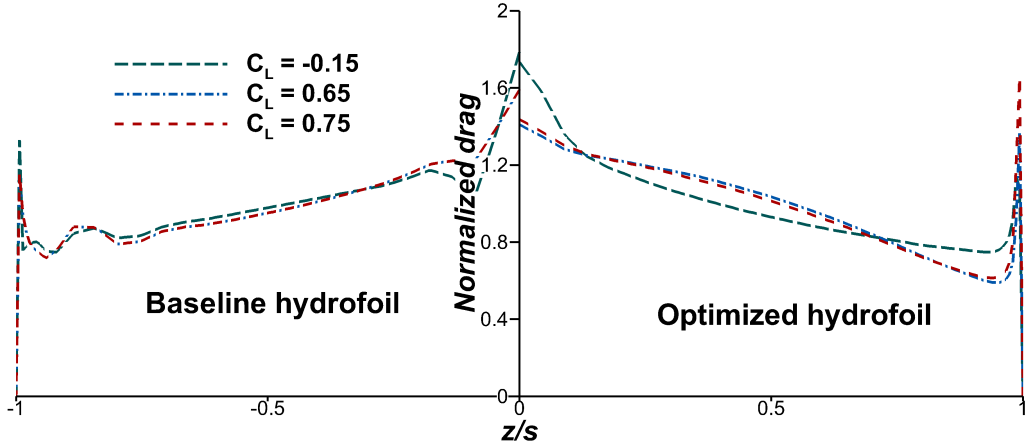


Figure 10: Comparison of the predicted spanwise normalized drag distribution for the NACA 0009 baseline, and the multipoint optimized design at  $C_L = -0.15$ ,  $C_L = 0.65$ , and  $C_L = 0.75$ . The comparison of the resulting drag coefficient is listed in Table 4.

by the much improved performance of the optimized hydrofoil captured by both the measurements and predictions.

#### <sup>410</sup> 6.2.2. Cavitation Performance Comparison

In this section, we compare the cavitating performance of the optimized aluminum hydrofoil to the baseline stainless steel hydrofoil using experimental measurements and observations for  $\alpha = 6^\circ$  and  $Re = 0.8 \times 10^6$ . The hydrofoil was optimized to avoid cavitation for  $Re = 10^6$  for  $-0.15 \leq C_L \leq 0.75$  and  $\sigma \geq 1.6$ . Based on the numerical predictions, cavitation should inception later (i.e., at a lower  $\sigma$ ) for the optimized hydrofoil compared to the baseline. Ideally, cavitation performance should be compared between hydrofoils made with the same material, at the same

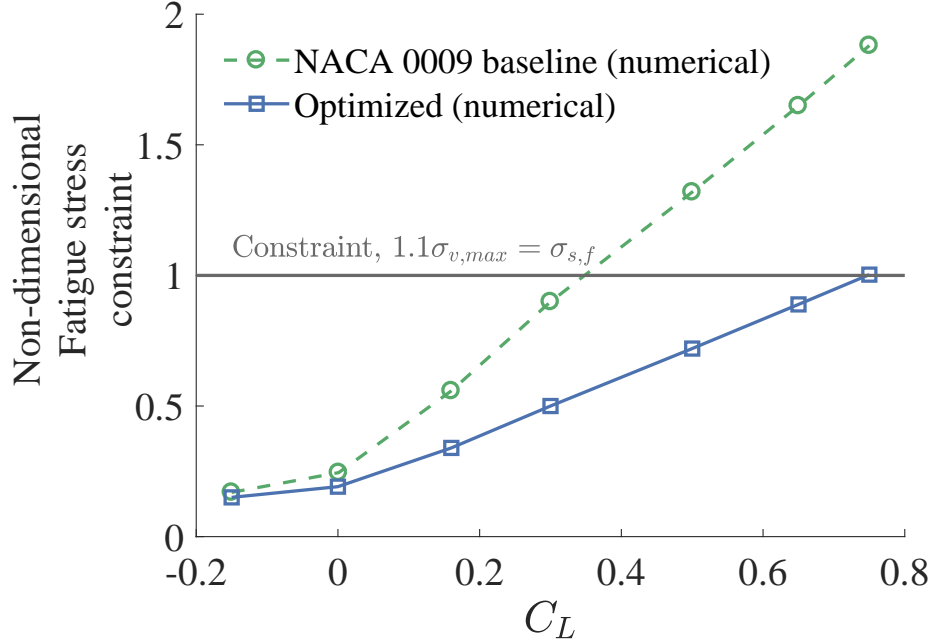


Figure 11: While the aluminum NACA 0009 baseline hydrofoil does not meet the stress constraint for  $C_L \geq 0.35$ , the multipoint hydrostructural optimized aluminum hydrofoil meets the stress constraint up to  $C_L = 0.75$ , the highest expected loading condition.

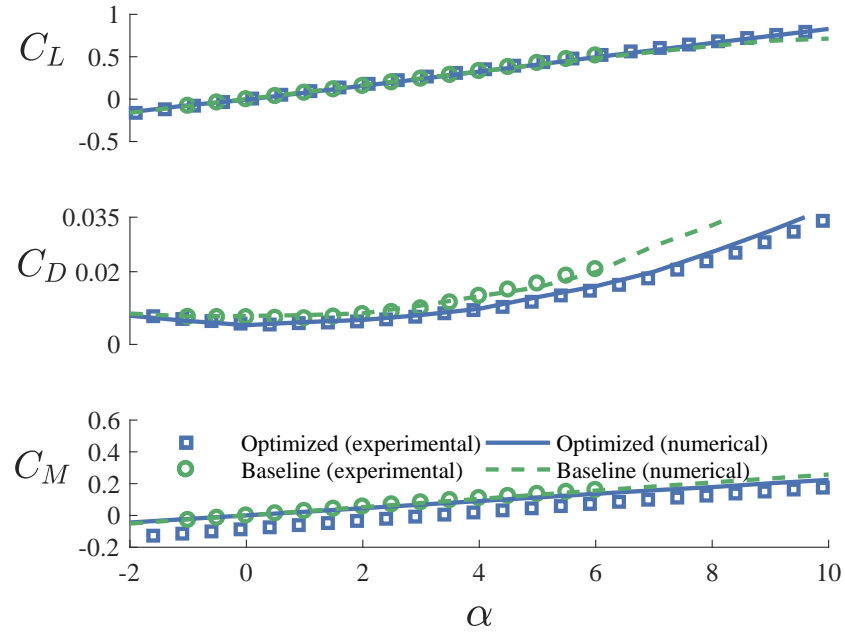


Figure 12: Predicted and measured values of the mean  $C_L$ ,  $C_D$ , and  $C_M$  for the baseline hydrofoil and the optimized hydrofoil. The differences between the numerical predictions and the experimental measurements are listed in Table 5.

cavitation number, lift coefficient, and Reynolds number. While the Reynolds number used for the predictions was  $10^6$ , the experimental measurements for both the baseline and optimized hydrofoils were conducted at Reynolds number of  $0.8 \times 10^6$  for all the cavitation studies.

The experimental conditions for the cavitation tunnel testing of the baseline and optimized

Table 5: Difference between the numerical predictions and the experimental measurements for the optimized hydrofoil.

Hydrodynamic coefficient	Maximum error [%]	Mean error [%]	Minimum error [%]
$C_L$	6.12	2.96	0.33
$C_D$	10.44	5.10	0.30
$C_M$	9.72	3.00	0.35
$\delta_{\text{tip}}$	10.40	3.45	0.50

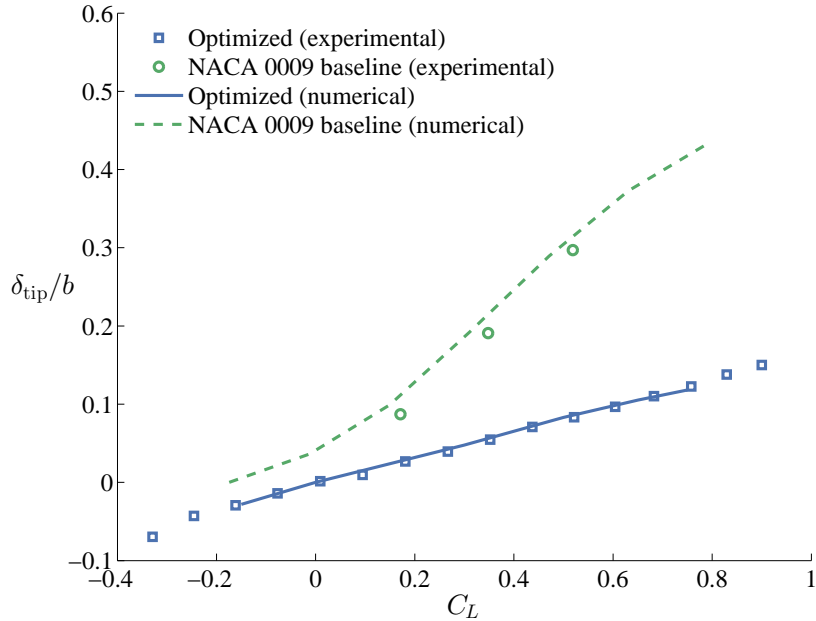


Figure 13: Predicted and measured values of the steady-state tip bending deflection,  $\delta_{\text{tip}}$ , for the baseline aluminum NACA 0009 hydrofoil and the multipoint optimized aluminum hydrofoil. The mean difference in the tip deflections is 3.45%.

hydrofoils are listed in Table 6. It should be noted that the cavitating runs were meant to be exploratory runs only, and hence the test conditions were not ideal. However, we realized after the test that the data from the exploratory run was enough to perform a valuable qualitative cavitation performance comparison, which confirmed that cavitation inception was significantly delayed for the optimized hydrofoil. Note that additional cavitation tests could not be conducted because tunnel time and project budget limitations. An accurate quantitative cavitation performance comparison would require further experiments in the future. Nevertheless, the use of the baseline stainless steel hydrofoil instead of the aluminum hydrofoil with a slightly different Reynolds numbers have a minimal impact on the results, because as shown in the experimental results by Zarruk et al. [15], the differences between the performance of the baseline stainless steel hydrofoil at  $\text{Re} = 0.8 \times 10^6$  and the aluminum hydrofoil at  $\text{Re} = 10^6$  are negligible. Based on the experimental measurements presented in [15], the mean difference in  $C_L$  between these two cases is 3.4%.

Since the baseline stainless steel hydrofoil and the optimized aluminum hydrofoil were tested at the same geometric angle of attack, they exhibit different lift coefficients because of the different twist distributions and cross-sectional shapes. In hindsight, the optimized hydrofoil and the base-

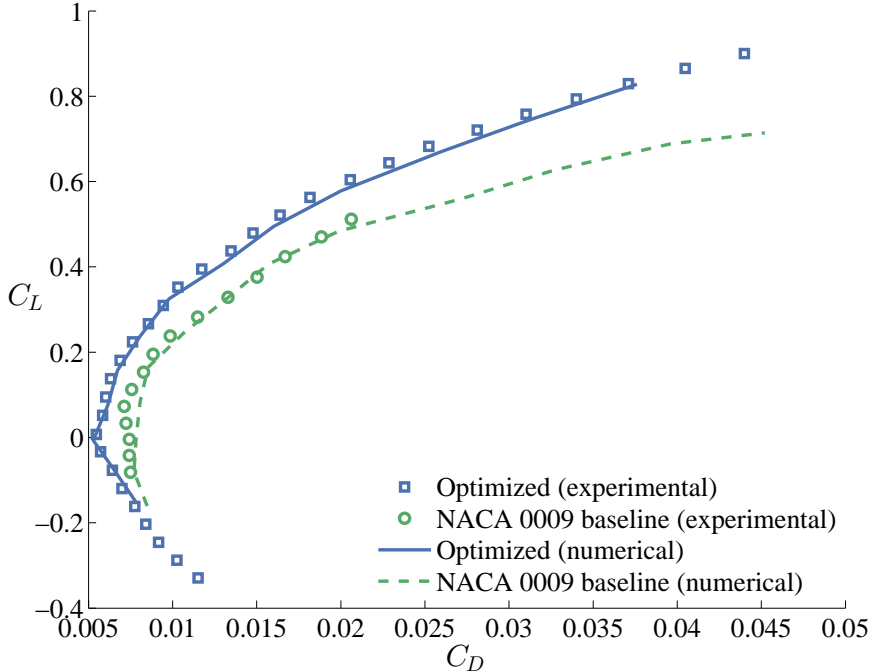


Figure 14: Predicted and measured drag polar for the baseline NACA 0009 hydrofoil and the multipoint optimized hydrofoil. Both predictions and measurements show that the optimized hydrofoil has lower drag value as compared to the baseline for the entire range of lift conditions.

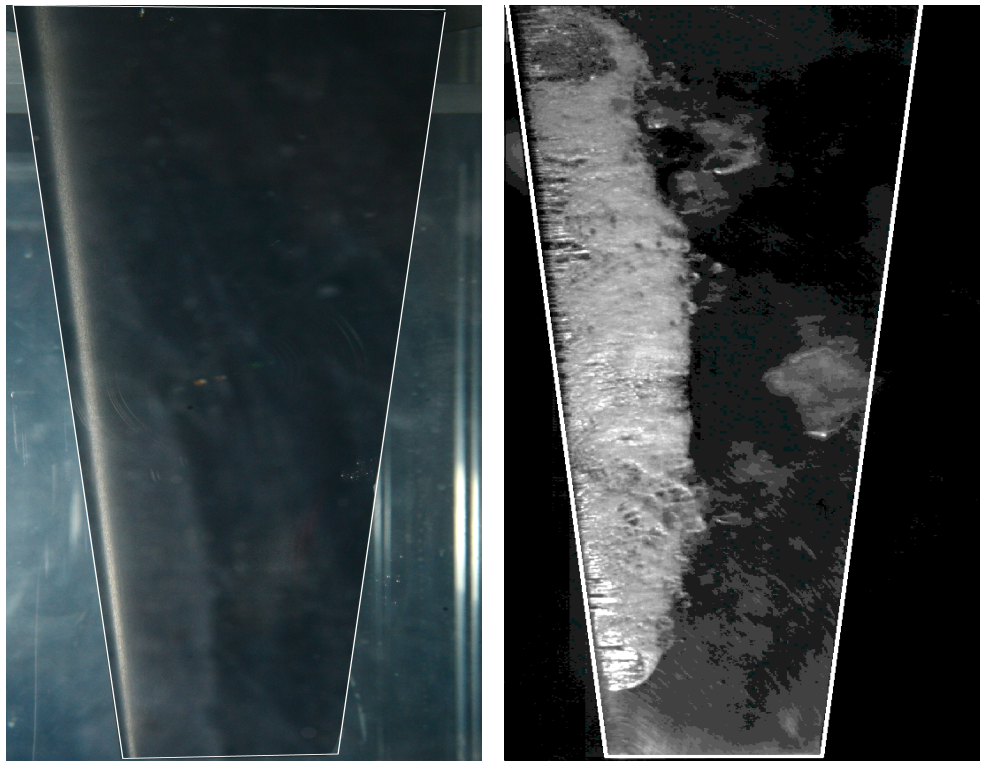
line hydrofoil should be tested at the same fully wetted lift coefficient. Nevertheless, the influence of the different lift coefficients can be removed by normalizing the instantaneous cavitating lift coefficients by its fully wetted values. Figures 15 and 16 show the baseline and optimized hydrofoils for two different cavitation numbers:  $\sigma \approx 1.0$  and  $\sigma \approx 0.8$ .

Table 6: Cavitation tunnel experimental conditions for the baseline and the optimized hydrofoils.

Parameter	Baseline hydrofoil	Optimized hydrofoil	Impact
Material	Stainless steel	Aluminum	Minimal
$C_L$	0.52	0.49	Minimal
Re	$0.8 \times 10^6$	$0.8 \times 10^6$	Minimal
$\sigma$	2.0, 1.5, 1.0, 0.9, 0.8, 0.7, 0.6, 0.5, 0.4, 0.3, 0.25	2.5, 2.1, 1.8, 1.7, 1.6, 1.5, 1.4, 1.1, 0.95, 0.75	Significant

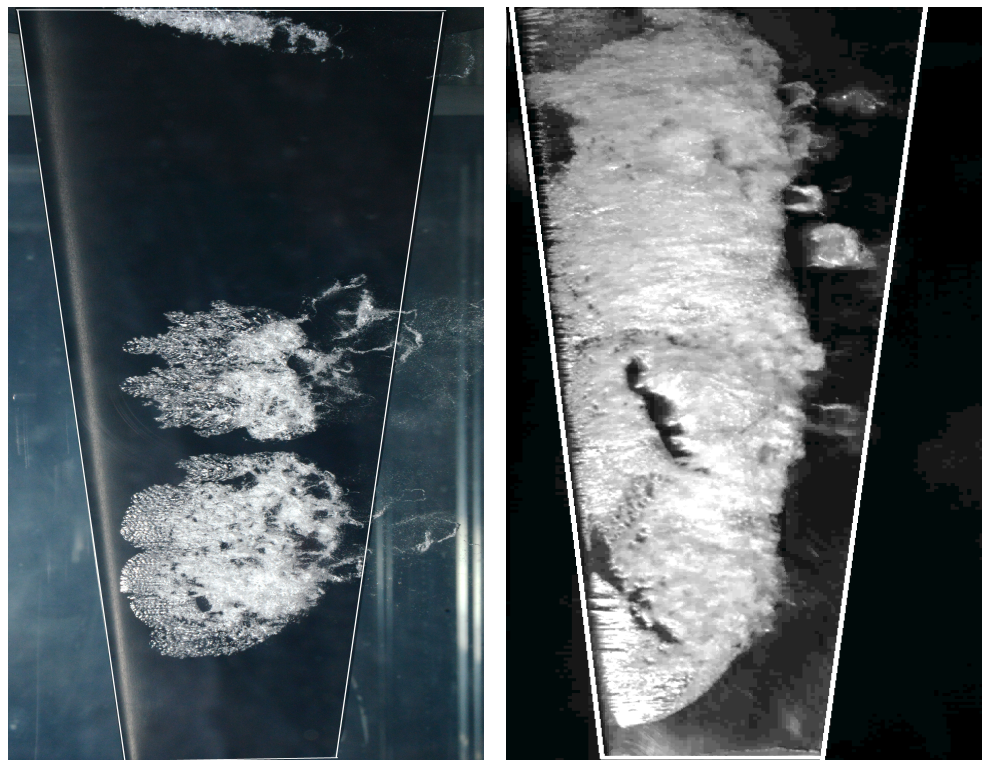
Figure 15 shows that while the baseline hydrofoil exhibits leading edge partial cavitation with a maximum cavity length around 40% of the chord length at  $\sigma = 1.0$  and  $C_L = 0.52$ , cavitation could not be detected on the optimized hydrofoil even at  $\sigma = 0.95$  and  $C_L = 0.49$ . Figure 16 compares the extent of cavitation for the optimized hydrofoil and the baseline hydrofoil at  $\sigma$  of 0.75 and 0.8, respectively. The results show much greater cavitation extent for the baseline hydrofoil compared to the optimized one at nominally equivalent flow conditions.

In addition to the cavitation extent shown in the images, the cavitation performance can also be quantified using the unsteady lift coefficients. In Figure 17, the maximum, mean, and minimum



(a) Optimized hydrofoil;  $\sigma = 0.95$ ;  $C_L = 0.49$ . (b) Baseline NACA 0009 hydrofoil;  $\sigma = 1.0$ ;  $C_L = 0.52$ .

Figure 15: While the baseline hydrofoil shows significant partial leading edge cavitation with a maximum cavity length around 40% of the chord length, no cavitation is observed for the optimized hydrofoil at similar  $\sigma$  and  $C_L$  values.  $Re = 0.8 \times 10^6$ ;  $\alpha = 6^\circ$ .



(a) Optimized hydrofoil;  $\sigma = 0.75$ ;  $C_L = 0.49$ . (b) Baseline NACA 0009 hydrofoil;  $\sigma = 0.8$ ;  $C_L = 0.52$ .

Figure 16: For similar  $\sigma$  and  $C_L$  values, there is much less cavitation on the optimized hydrofoil compared to the baseline hydrofoil.  $Re = 0.8 \times 10^6$ ;  $\alpha = 6^\circ$ .

values of  $C_L/C_{L\text{wet}}$  are plotted against  $\sigma$  for the baseline and optimized hydrofoils.  $C_L$  is the instantaneous lift coefficient, which fluctuates with time due to unsteady cavity shedding, and  $C_{L\text{wet}}$   
450 is the mean lift coefficient for the fully-wetted condition, i.e., no cavitation. We plot  $C_L/C_{L\text{wet}}$  to remove differences in  $C_L$ . For mean  $C_L \approx 0.5$ ,  $C_L/C_{L\text{wet}} \approx 1$  for  $\sigma > 1.5$ , because the flow is fully attached and fully wetted. The mean  $C_L$  increases marginally with the onset of partial leading edge cavitation due to increase in effective camber caused by the formation of a leading edge cavitating vortex, then decreases as the cavitation number  $\sigma$  further reduces due to limitation of the suction side pressure by the vapor pressure. The inception of cavitation is also denoted by unsteady dynamic load fluctuations due to periodic growth and shedding of the cavity [44]. As shown by Akcabay et al. [45], the amplitude of the unsteady load fluctuation reaches a maximum when the maximum extent of the cavity reaches near the hydrofoil trailing edge. As  $\sigma$  further reduces, the cavity length further increases and extends well beyond the hydrofoil trailing edge, the amplitude of the unsteady load fluctuations reduces until relatively stable supercavitation develops [44].  
460

Hence, changes in the difference between maximum and minimum values of the unsteady lift coefficient indicate cavitation development for cases with uniform flow and low inlet turbulent intensity, such as examined here. Figure 17 shows that for similar  $C_L/C_{L\text{wet}}$  values, significant fluctuations of the hydrodynamic loads for the baseline hydrofoil occur for  $\sigma \lesssim 1.0$ , which is a good indication of cavitation development, while no significant fluctuations are observed for the optimized hydrofoil until  $\sigma = 0.75$ .

Figure 18 compares the time history for  $C_L/C_{L\text{wet}}$  at various cavitation numbers for both the baseline and the optimized hydrofoils. The results show that while the baseline hydrofoil has significantly higher fluctuations at  $\sigma = 0.9$ , the optimized hydrofoil has minimal fluctuations  
470 because there was no cavitation at  $\sigma = 0.95$ , as shown in Figure 15. Given the results shown in Figures 15 to 18, we conclude that the optimized hydrofoil demonstrated delayed cavitation inception compared to the baseline hydrofoil. Nevertheless, additional cavitating measurements would be required to quantify the exact improvements.

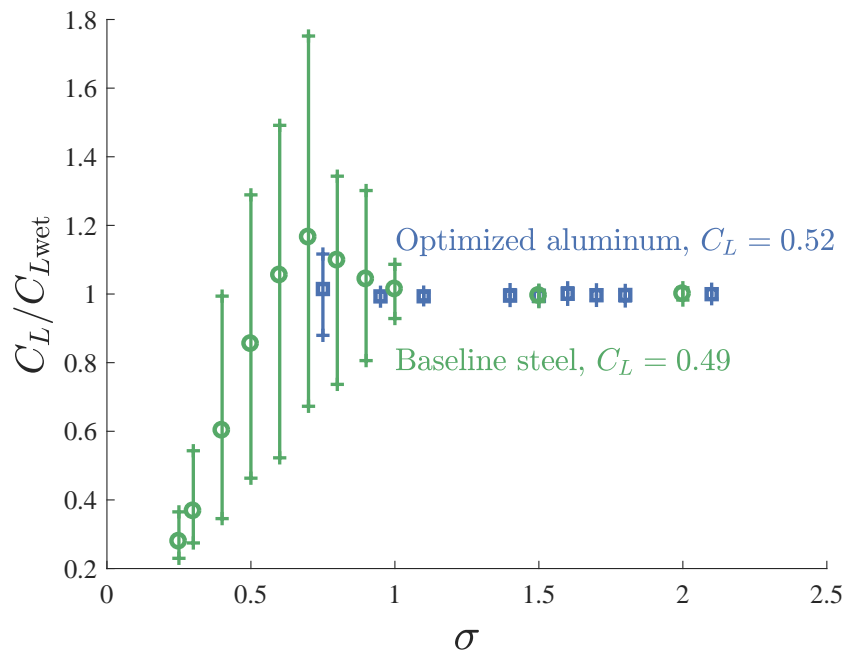
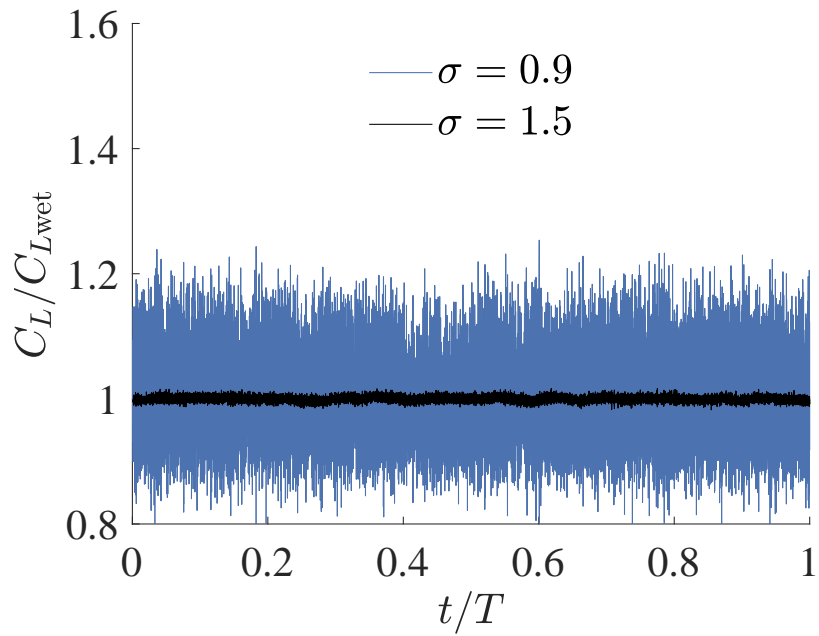
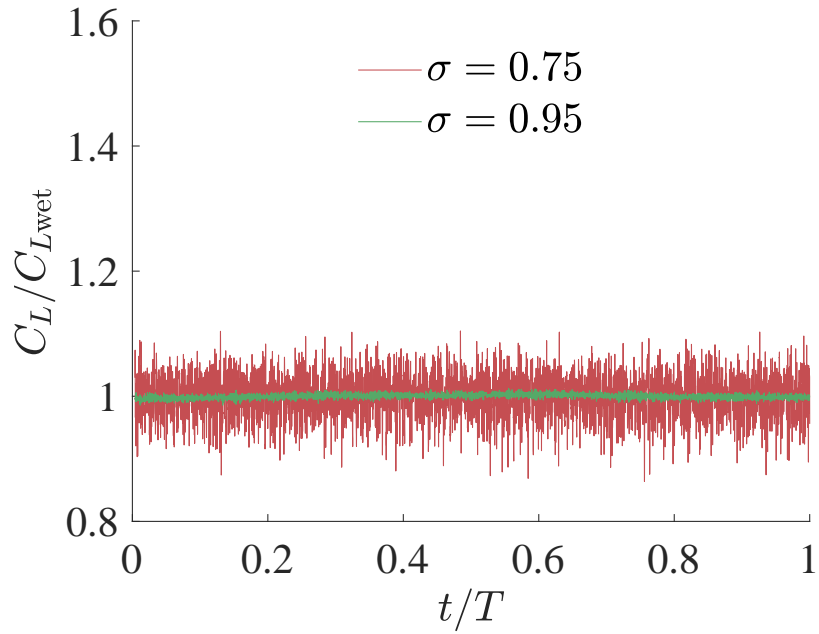


Figure 17: Comparison of maximum, minimum, and mean values of  $C_L/C_{Lwet}$  as a function of the cavitation number ( $\sigma$ ) for the baseline stainless steel hydrofoil (green/light) and the optimized hydrofoil (blue/dark). Note that for a similar  $C_L/C_{Lwet}$ , unsteady load fluctuations due to periodic growth and shedding of cavitation occurs earlier (i.e. at a higher  $\sigma$ ) for the baseline hydrofoil compared to the optimized hydrofoil.



(a) Baseline NACA 0009 hydrofoil (steel)



(b) Optimized hydrofoil

Figure 18: Time history of measured non-dimensional lift coefficient for the baseline hydrofoil at  $C_L = 0.52$  (top) and the optimized hydrofoil at  $C_L = 0.49$  (bottom) for various cavitation numbers. Note that while the baseline hydrofoil shown significant cavity-induced unsteady load fluctuation at  $\sigma = 0.9$ , the optimized hydrofoil exhibit no cavitation at  $\sigma = 0.95$ , as indicated by the relatively steady instantaneous  $C_L$  values, and confirmed by the photographs shown in Figure 15.

## 7. Conclusions

In this paper, we address the need for experimental validation of optimized marine lifting surfaces by manufacturing and testing the baseline and the optimized hydrofoil proposed by Garg et al. [1]. Garg et al. [1] carried out multipoint hydrostructural optimization for a cantilevered aluminum NACA 0009 tapered hydrofoil with no sweep at  $Re = 10^6$  and  $U = 12.4 \text{ m/s}$ . They used 210 shape design variables representing the hydrofoil camber, thickness, and twist distributions, with constraints on lift coefficients, hydrofoil planform, stress, cavitation, and minimum trailing edge thickness. Garg et al. [1] showed that hydrodynamic-only optimization leads to a slightly more efficient design with very different optimized geometry compared to the hydrostructural optimization, but hydrodynamic-only design does not satisfy the stress constraints. Thus, coupled hydrostructural optimization is needed to acquire a physically realizable design, and to avoid unwanted flow-induced vibration and instability issues.

While coarser CFD and FEA meshes were used in the optimization in favor of computational efficiency, a finer CFD and FEA meshes was used for the validation studies shown here to ensure accuracy. Good agreement was observed between the predicted and the measured values of the hydrodynamic coefficients ( $C_L$ ,  $C_D$ , and  $C_M$ ) and the tip bending deflections ( $\delta_{\text{tip}}$ ) for both the baseline and the optimized hydrofoils across a wide range of lift conditions. For the optimized hydrofoil, the mean difference between the predicted and measured values for mean  $C_L$ ,  $C_D$ , and  $C_M$  was 2.96%, 5.10%, and 3.0%, respectively. The mean difference in the tip bending deflections was 3.45%.

The results also confirmed the significant improvement in the lift-to-drag ratio for the optimized hydrofoil compared to the baseline across the full range of  $C_L$  from  $-0.15$  to  $0.75$ , even with an increase in mass of 41.5% due to the thicker cross-sections. **The measured improvement in efficiency at  $C_L = 0.3$  is 46.8%, and at  $C_L = 0.65$  is 23.9%, while the corresponding predicted improvements are 31.6% and 40.0%. The improvements in efficiencies are much higher than the measurement uncertainty of 0.95 – 1.2% for the hydrodynamic loads. The improvement in efficiency is also much greater than the error of 0.30 – 10.44% between the predicted and measured hydrodynamic load coefficients.**

The results show that the tip bending deflection for the optimized aluminum hydrofoil is almost 67% lower than the bending deflection for the baseline aluminum hydrofoil for  $C_L \geq 0.3$ . In addition, the natural frequencies of the optimized aluminum hydrofoil are also significantly higher than the baseline aluminum hydrofoil. The results are consistent with the predictions, which showed that the thinner baseline hydrofoil violates the stress constraint for  $C_L \geq 0.35$ , while the thicker optimized hydrofoil satisfies the fatigue strength constraint up to the highest loading condition of  $C_L = 0.75$ .

The cavitation performance of the optimized hydrofoil was also investigated experimentally. While the experimental cavitation results were mostly qualitative, comparisons of the observed cavitation patterns and unsteady lift coefficients suggest significantly delayed cavitation inception for the optimized hydrofoil compared to the baseline hydrofoil. For a more detailed quantitative analysis of cavitating performance, additional cavitation testing comparing the baseline and optimized hydrofoil made of the same material and tested for the same range of lift conditions and cavitation numbers would be required in the future.

The results presented herein confirm that the hydrostructural design optimization approach results in realizable practical improved performance. The 29% improvement in the measured overall

efficiency against NACA 0009 baseline hydrofoil across lift coefficients ranging from -0.15 to 0.75 is impressive, particularly given the thicker section, the higher load capacity, and the much  
520 delayed cavitation inception characteristic of the optimized hydrofoil. Given the short design cycle for these coupled high-fidelity hydrostructural optimizations (less than 10 h using 1,000 processors), this approach has the potential to revolutionize the design of the next generation of advanced hydrofoils and marine propulsors.

## 8. Acknowledgments

Support for this research was provided by the U.S. Office of Naval Research (Contract N00014–16–1–2972), managed by Ms. Kelly Cooper. The authors wish to thank Mr. Robert Wrigley for his valuable help setting up the experiments.

## References

- [1] N. Garg, G. K. Kenway, J. R. Martins, Y. L. Young, High-fidelity multipoint hydrostructural optimization of a 3-d hydrofoil, *Journal of Fluids and Structures* 71 (2017) 15 – 39.  
530 doi:<https://doi.org/10.1016/j.jfluidstructs.2017.02.001>.  
URL <http://www.sciencedirect.com/science/article/pii/S088997461630144X>
- [2] J. R. R. A. Martins, A. B. Lambe, Multidisciplinary design optimization: A survey of architectures, *AIAA Journal* 51 (9) (2013) 2049–2075. doi:[10.2514/1.J051895](https://doi.org/10.2514/1.J051895).
- [3] D. Peri, M. Rossetti, E. F. Campana, Design optimization of ship hulls via CFD techniques, *Journal of Ship Research* 45 (2) (2001) 140–149.
- [4] D. Peri, E. F. Campana, Multidisciplinary design optimization of a naval surface combatant, *Journal of Ship Research* 47 (1) (2003) 1–12.
- 540 [5] E. F. Campana, D. Peri, Y. Tahara, F. Stern, Shape optimization in ship hydrodynamics using computational fluid dynamics, *Computer Methods in Applied Mechanics and Engineering* 196 (1) (2006) 634–651.
- [6] Y. Tahara, S. Tohyama, T. Katsui, CFD-based multi-objective optimization method for ship design, *International Journal for Numerical Methods in Fluids* 52 (5) (2006) 499–527.
- [7] C. Lin, Y. Lee, C. Hung, Optimization and experiment of composite marine propellers, *Composite Structures* 89 (2) (2009) 206–215.
- [8] M. Motley, Z. Liu, Y. Young, Utilizing fluid–structure interactions to improve energy efficiency of composite marine propellers in spatially varying wake, *Composite Structures* 90 (3) (2009) 304–313.
- 550 [9] Y. Lee, C. Lin, Optimized design of composite propeller, *Mechanics of advanced materials and structures* 11 (1) (2004) 17–30.

- [10] J. P. Blasques, C. Berggreen, P. Andersen, Hydro-elastic analysis and optimization of a composite marine propeller, *Marine Structures* 23 (1) (2010) 22–38.
- [11] Y. L. Young, M. R. Motley, R. Barber, E. J. Chae, N. Garg, Adaptive composite marine propulsors and turbines: Progress and challenges, *Applied Mechanics Reviews* 68 (6) (2016) 060803.
- [12] J. R. R. A. Martins, J. T. Hwang, Review and unification of methods for computing derivatives of multidisciplinary computational models, *AIAA Journal* 51 (11) (2013) 2582–2599. doi:10.2514/1.J052184.
- 560 [13] G. K. W. Kenway, G. J. Kennedy, J. R. R. A. Martins, Scalable parallel approach for high-fidelity steady-state aeroelastic analysis and derivative computations, *AIAA Journal* 52 (5) (2014) 935–951. doi:10.2514/1.J052255.
- [14] A. Ducoin, J. A. Astolfi, M. Gobert, An experimental study of boundary-layer transition induced vibrations on a hydrofoil, *Journal of Fluids and Structures* 32 (2012) 37–51.
- [15] G. Zarruk, P. Brandner, B. Pearce, A. W. Phillips, Experimental study of the steady fluid-structure interaction of flexible hydrofoils, *Journal of Fluids and Structure* 51 (2014) 326–343.
- 570 [16] D. T. Akcabay, Y. L. Young, A. Lelong, J. A. Astolfi, Cavity-induced vibrations of flexible hydrofoils and their susceptibility to lock-in and parametric excitations, in: Proceedings of the 2014 Symposium on Naval Hydrodynamics, 2014.
- [17] D. T. Akcabay, E. J. Chae, Y. L. Young, A. Ducoin, J. A. Astolfi, Cavity induced vibration of flexible hydrofoils, *Journal of Fluids and Structures* 49 (2014) 463–484.
- [18] S. Gowing, P. Coffin, C. Dai, Hydrofoil cavitation improvements with elastically coupled composite materials, in: Proceedings of the 25th American Towing Tank Conference, 1998.
- [19] B. Chen, S. Neely, T. Michael, S. Gowing, R. Szwerc, D. Buchler, R. Schult, Design, fabrication and testing of pitch-adapting (flexible) composite propellers, in: The SNAME Propellers/Shafting Symposium '06, Virginia Beach, VA, 2006.
- [20] B. Paik, G. Kim, K. Kim, H. Seol, B. Hyun, S. Lee, Y. Jung, Investigation on the performance characteristics of the flexible propellers, *Ocean Engineering* 73 (2013) 139–148.
- 580 [21] Y. Lee, C. Lin, Regression of the response surface of laminated composite structures, *Composite structures* 62 (1) (2003) 91–105.
- [22] C. Lin, Y. Lee, Stacking sequence optimization of laminated composite structures using genetic algorithm with local improvement, *Composite structures* 63 (3) (2004) 339–345.
- [23] M. Herath, Optimization of composite marine propeller blades and hydrofoils, Ph.D. thesis, School of Mechanical and Manufacturing Engineering, University of New South Wales, Australia (2015).

- [24] M. T. Herath, B. G. Prusty, A. W. Phillips, N. St John, Structural strength and laminate optimization of self-twisting composite hydrofoils using a genetic algorithm, *Composite Structures*.
- 590 [25] G. K. W. Kenway, J. R. R. A. Martins, Multipoint high-fidelity aerostructural optimization of a transport aircraft configuration, *Journal of Aircraft* 51 (1) (2014) 144–160. doi:10.2514/1.C032150.
- [26] R. E. Perez, P. W. Jansen, J. R. R. A. Martins, pyOpt: A Python-based object-oriented framework for nonlinear constrained optimization, *Structural and Multidisciplinary Optimization* 45 (1) (2012) 101–118. doi:10.1007/s00158-011-0666-3.
- [27] E. van der Weide, G. Kalitzin, J. Schluter, J. J. Alonso, Unsteady turbomachinery computations using massively parallel platforms, in: *Proceedings of the 44th AIAA Aerospace Sciences Meeting and Exhibit*, Reno, NV, 2006, AIAA 2006-0421.
- 600 [28] P. Spalart, S. Allmaras, A one-equation turbulence model for aerodynamic flows, in: *30th Aerospace Sciences Meeting and Exhibit*, 1992. doi:10.2514/6.1992-439.  
URL <http://dx.doi.org/10.2514/6.1992-439>
- [29] N. Garg, G. K. W. Kenway, Z. Lyu, J. R. R. A. Martins, Y. L. Young, High-fidelity hydrodynamic shape optimization of a 3-D hydrofoil, *Journal of Ship Research* 59 (4) (2015) 209–226. doi:10.5957/JOSR.59.4.150046.
- [30] N. Garg, Z. Lyu, T. Dhert, J. R. R. A. Martins, Y. L. Young, High-fidelity hydrodynamic shape optimization of a 3-D morphing hydrofoil, in: *Fourth International Symposium on Marine Propulsors*, Houston, USA, 2015.
- [31] A. Jameson, W. Schmidt, E. Turkel, Numerical solutions of the Euler equations by finite volume methods using Runge–Kutta time-stepping schemes, *AIAA paper* (1981) 1259.
- 610 [32] G. J. Kennedy, J. R. R. A. Martins, A parallel finite-element framework for large-scale gradient-based design optimization of high-performance structures, *Finite Elements in Analysis and Design* 87 (2014) 56–73. doi:10.1016/j.finel.2014.04.011.
- [33] G. A. Wrenn, An indirect method for numerical optimization using the Kreisselmeier–Steinhauser function, *Tech. Rep. CR-4220*, NASA (1989).
- [34] A. B. Lambe, J. R. R. A. Martins, G. J. Kennedy, An evaluation of constraint aggregation strategies for wing box mass minimization, *Structural and Multidisciplinary Optimization* 55 (1) (2016) 257–277. doi:10.1007/s00158-016-1495-1.
- [35] S. A. Brown, Displacement extrapolation for CFD + CSM aeroelastic analysis, *AIAA paper 1090* (1997).
- 620 [36] P. E. Gill, W. Murray, M. A. Saunders, SNOPT: An SQP algorithm for large-scale constrained optimization, *SIAM Journal of Optimization* 12 (4) (2002) 979–1006. doi:10.1137/S1052623499350013.

- [37] P. A. Brandner, Y. Lecoffre, G. J. Walker, Design considerations in the development of a modern cavitation tunnel, In: Proceedings of the 18th Australian Fluid Mechanics Conference (2007) 630–637.
- [38] C. Doolan, P. Brandner, D. Butler, B. Pearce, D. Moreau, L. Brooks, Hydroacoustic characterisation of the AMC cavitation tunnel, in: Proceedings of Acoustics, 2013.
- [39] M. S. Selig, J. J. Guglielmo, A. P. Broeren, P. Giguere, Experiments on airfoils at low Reynolds numbers, AIAA Paper 62.
- 630 [40] I. H. Abbott, A. E. Von Doenhoff, L. Stivers Jr, Summary of airfoil data, NACA Technical Report 824, 1945.
- [41] E. N. Jacobs, A. Sherman, Airfoil section characteristics as affected by variations of the Reynolds number, NACA Report 586. National Advisory Committee for Aeronautics.
- [42] Y. L. Young, N. Garg, P. A. Brandner, B. W. Pearce, D. Butler, D. Clarke, A. W. Phillips, Load-dependent bend-twist coupling effects on the steady-state hydroelastic response of composite hydrofoils, Composite Structures, 2017.
- [43] MATLAB, R2013b, The MathWorks Inc., Natick, Massachusetts, 2013.
- [44] Y. Young, C. Harwood, F. M. Montero, J. Ward, S. Ceccio, Ventilation of lifting bodies: Review of the physics and discussion of scaling effects, Applied Mechanics Reviews 69 (1).
- 640 [45] D. T. Akcabay, Y. L. Young, Parametric excitations and lock-in of flexible hydrofoils in two-phase flows, Journal of Fluids and Structures 57 (2015) 344–356.